Asymmetry effects driving secondary instabilities in two-dimensional collisionless magnetic reconnection

D. Grasso, D. Borgogno, E. Tassi, A. Pérona

▶ **To cite this version:**

D. Grasso, D. Borgogno, E. Tassi, A. Pérona. Asymmetry effects driving secondary instabilities in two-dimensional collisionless magnetic reconnection. Physics of Plasmas, 2020, 27, pp.012302. 10.1063/1.5125122 . hal-02890499

HAL Id: hal-02890499
https://hal.science/hal-02890499

Submitted on 6 Jul 2020

HAL is a multi-disciplinary open access archive for the deposit and dissemination of scientific research documents, whether they are published or not. The documents may come from teaching and research institutions in France or abroad, or from public or private research centers.

L'archive ouverte pluridisciplinaire **HAL**, est destinée au dépôt et à la diffusion de documents scientifiques de niveau recherche, publiés ou non, émanant des établissements d'enseignement et de recherche français ou étrangers, des laboratoires publics ou privés.

Asymmetry effects driving secondary instabilities in two-dimensional collisionless magnetic reconnection

D. Grasso[1], D. Borgogno[1], E. Tassi[2], A. Perona[3]

[1] *Istituto dei Sistemi Complessi - CNR and Dipartimento di Energia, Politecnico di Torino, Torino 10129, Italy*

[2] *Université Côte d'Azur, CNRS, Observatoire de la Côte d'Azur, Laboratoire J.L. Lagrange, Boulevard de l'Observatoire, CS 34229, 06304 Nice Cedex 4, France*

[3] *Dipartimento di Energia, Politecnico di Torino, Torino 10129, Italy*

(Dated: December 5, 2019)

Abstract

In the framework of the studies on magnetic reconnection, much interest has been recently devoted to asymmetric magnetic configurations, which can naturally be found in solar and astrophysical environments as well as in laboratory plasmas. Several aspects of this problem have been investigated, mainly in a two-dimensional geometry and by means of Particle-in-Cell simulations. Still, there are open questions concerning the onset and the effects of secondary instabilities in the nonlinear phase of an asymmetric reconnection process. In this work we focus on the conditions that lead to the appearance of the Kelvin-Helmholtz instability following an asymmetric reconnection event in a collisionless plasma. The investigation is carried out by means of two-dimensional numerical simulations based on a reduced fluid model assuming a strong guide field. We show that, unlike the symmetric case, in the presence of asymmetry, a Kelvin-Helmholtz-like instability can develop also for a finite equilibrium electron temperature. In particular, simulations indicate the formation of steep velocity gradients, which drive the instability, when the resonant surface of the equilibrium magnetic field is located sufficiently far from the peak of the equilibrium current density. Moreover, a qualitative analysis of the vorticity dynamics shows that the turbulent behavior induced by the secondary instability is not confined inside the island but can also affect the plasma outside the separatrices. The comparison between simulations carried out with an adiabatic closure and a Landau-fluid closure for the electron fluid, indicates that the latter inhibits the secondary instability by smoothing velocity gradients.

I. INTRODUCTION

Magnetic reconnection (MR) is a change in the topology of the magnetic field, usually accompanied by a fast conversion of magnetic energy into plasma kinetic energy and heat,as well as by a release of accelerated particles following the formation of intense current and vorticity layers (also referred to as sheets, in the literature and in the present paper). Due to its relevance in a wide variety of physical phenomena ranging from space to laboratory plasmas, MR has benefit of a vast amount of studies [4, 31] since the formulation of the first model by Sweet and Parker [26, 35]. In the past three decades much attention has been paid to the problem of fast reconnection. Starting in the 90's many studies [2, 3, 25, 38] focused on the physical mechanisms that can drive fast reconnection in high temperature and low collisional plasmas. Electron inertia became the first candidate to explain the occurrence of MR in this context, where, in the absence of dissipation, the topological constraint on the magnetic field is transferred to generalized fields associated with infinite families of Casimirs invariants, while the topological transition in the magnetic field leads to a continuous cascade of energy towards small scales, thus causing the narrowing of the current and vorticity layers. It is namely MR caused by electron inertia that we will consider in our analysis.

When the spectrum of the magnetic field is dominated by a single mode, the study of MR can be carried out under the two-dimensional (2D) approximation. In such 2D framework it is possible to distinguish between two different configurations, depending on the presence of finite gradients of the equilibrium current density at the resonant surface, where the MR instability develops: a symmetric one, in which the peak of the current density is located at the resonant surface and an asymmetric configuration where the peak is not located at the resonant surface.

The symmetric case has been extensively studied, analytically and numerically, in the linear and nonlinear regimes [4]. At the beginning of the 2000s a number of works based on reduced fluid models, which are suitable when a strong component of the magnetic field in one direction is present, were devoted to the nonlinear evolution of the current and

vorticity sheets in symmetric configurations in the cold ion limit and for large values of the standard instability parameter Δ' [13]. In particular, these works focused on the onset of secondary instabilities of the fluid type, like the Kelvin Helmholtz (KH) one, occurring nonlinearly on top of a MR instability and leading to the generation of turbulence in the current and vorticity sheets. In the low-β_e limit, with β_e indicating the ratio between the equilibrium kinetic pressure of the electrons and the magnetic pressure of the guide field, past studies carried out in this context [9–11, 14] agreed on two points. In the first place, it is possible to develop secondary fluid-like instabilities only when the electron temperature is negligible (or, more in general, when $\rho_s \ll d_e$, with ρ_s indicating the ion sound Larmor radius and d_e the electron skin depth). In the second place, the fluid-like instability develops inside the magnetic island generated by the MR process. Still in the context of symmetric reconnection, further studies, based on reduced fluid models, showed that secondary KH-like instabilities develop in the plasma vorticity also in the presence of finite electron temperature, provided that β_e is sufficiently high [15, 37].

How the current and vorticity layers are affected by such secondary instabilities in an asymmetric configuration is still an open question, in spite of the relevance of MR in asymmetric systems. Indeed, the asymmetric case is important for instance in strongly driven, laser-generated plasmas [32] and in the framework of Tokamak physics, due to the fact that gradients of the current density at the rational surface naturally occur in toroidal and cylindrical geometry [1, 23, 24]. The asymmetric problem has recently been studied also in endogenous reconnection processes relevant to the electron temperature heating in a fusion burning plasma [8]. A renewed interest in the asymmetric configurations was also generated, after 2015 by the observations in the subsolar magnetosheath region [29] and from the Magnetosphere Multiscale Spacecraft (MMS), of reconnection occurring at the Earth's dayside between the solar wind and the Earth magnetic field, where the asymmetry arises both from the different plasma densities on the two sides of the reconnecting layers and from the configuration of the magnetic field itself [7]. Moreover, the KH instability has

been observed in conjunction with MR events in several astrophysical and space contexts such as in the magnetosphere, in the boundaries of the coronal mass ejections, in the solar corona and in the solar blowout jets (see Ref. [20] and references therein). Many numerical simulations have been devoted to this particular 2D asymmetric setting, aimed at highlighting the difference with a fully 3D system and explaining the data reported from the MMS mission [18, 30]. In these studies, mainly conducted using PIC codes, a lot of attention has been paid to the turbulence developing along the current density layers inside and around the magnetic island that forms during the reconnection event. The main result of these investigations is that secondary instabilities leading to turbulence may develop mainly when a fully 3D setting is considered, while the 2D configurations remain laminar.

The evolution of the narrow vorticity sheets following MR in asymmetric configurations is the subject of the present paper. We describe asymmetric MR by adopting the 2D limit of the reduced fluid model of Ref. [36], which accounts for the parallel temperature evolution and for Landau damping effects as well. The asymmetry is introduced in the equilibrium magnetic field, while no equilibrium density gradients are assumed. The basic idea of our approach is to reduce the problem to a few essential ingredients in order to evaluate the impact of the asymmetry on the stability of the current density and vorticity sheets. We will show that, contrary to what happens in the symmetric case, turbulence driven by KH-like instabilities may develop also when $d_e \leq \rho_s$. Moreover the turbulence, that in the symmetric case is confined inside the magnetic island, in the asymmetric case may cross the separatrix, opening new transport scenarios. We investigate the onset of the KH instability as a function of various parameters characterizing the equilibrium magnetic field. We find that the crucial parameter for the onset of the instability appears to be the ratio x_s/λ, between the distance x_s of the of the rational surface from the location of the peak of the equilibrium current density, and the equilibrium scale length λ. Finally, the effect of an electron Landau closure on the development of secondary instabilities is also studied.

The paper is organized as follows. In Sec. II the 2D reduced Landau-gyrofluid model is reviewed in its cold ion limit. In Sec. III, after introducing the numerical setup, we describe

the results of our analysis of secondary instabilities following asymmetric MR. We conclude in Sec. IV.

II. MODEL EQUATIONS

Our analysis is based on the following reduced fluid model for a plasma consisting of electrons and of a single ionized particle species:

$$\frac{\partial \nabla_\perp^2 \varphi}{\partial t} + [\varphi, \nabla_\perp^2 \varphi] - \frac{2}{\beta_e}[A_\parallel, \nabla_\perp^2 A_\parallel] = 0, \tag{1}$$

$$\frac{\partial}{\partial t}\left(A_\parallel - \frac{2}{\beta_e}\delta^2 \nabla_\perp^2 A_\parallel\right) + [\varphi, A_\parallel - \frac{2}{\beta_e}\delta^2 \nabla_\perp^2 A_\parallel] + [A_\parallel, \nabla_\perp^2 \varphi] + [A_\parallel, t_{\parallel_e}] = 0, \tag{2}$$

$$\frac{\partial t_{\parallel_e}}{\partial t} + [\varphi, t_{\parallel_e}] - [A_\parallel, q_{\parallel_e}] - \frac{4}{\beta_e}[A_\parallel, \nabla_\perp^2 A_\parallel] = 0. \tag{3}$$

In Eqs. (1)-(3), the fields φ, $A_\parallel$, $t_{\parallel_e}$ and $q_{\parallel_e}$ are all functions of the time coordinate t and of the Cartesian spatial coordinates $(x, y) \in \mathcal{D} = \{(x, y) : -L_x \leq x \leq L_x, -L_y \leq y \leq L_y\}$, with L_x and L_y positive constants. Translational invariance of the system along the z coordinate of the Cartesian system is assumed.

The model equations (1)-(3) are formulated in terms of the following normalized variables:

$$\begin{aligned} &t = \Omega_i \hat{t}, \quad x = \frac{\hat{x}}{\rho_s}, \quad y = \frac{\hat{y}}{\rho_s}, \\ &\varphi = \frac{e\hat{\varphi}}{T_e}, \qquad A_\parallel = \frac{\hat{A}_\parallel}{B_0 \rho_s}, \qquad t_{\parallel_e} = \frac{\hat{t}_{\parallel_e}}{T_e}, \qquad q_{\parallel_e} = \frac{\hat{q}_{\parallel_e}}{n_0 T_e \rho_s \Omega_i}, \end{aligned} \tag{4}$$

where the caret symbol denotes dimensional quantities. We indicate with φ the electrostatic potential whereas $A_\parallel$ is the magnetic flux function, related to the normalized magnetic field $\mathbf{B}$ by $\mathbf{B}(x, y, t) = \nabla A_\parallel(x, y, t) \times \hat{z} + \hat{z}$, with $\hat{z}$ indicating the unit vector along the z direction. The model assumes indeed the presence of a constant and uniform component of the magnetic field (referred to as guide field) along the z direction. The amplitude of the guide field is assumed to be much larger than that of the x and y components of the magnetic field, i.e. $|\nabla A_\parallel| \ll 1$, for all $x, y \in \mathcal{D}$.

The fields $t_{\parallel_e}$ and $q_{\parallel_e}$ indicate the fluctuations of the electron temperature and heat flux, respectively, in the direction parallel to the guide field. In Eq. (4) we indicate with B_0 the

amplitude of the (dimensional) guide field, with T_e the constant and uniform equilibrium electron temperature, with e the proton charge and with n_0 the constant and uniform equilibrium particle density (equal for ions and electrons). The symbols Ω_i and ρ_s, on the other hand, refer to the ion cyclotron frequency based on the guide field, and to the ion sound Larmor radius, defined by $\rho_s = \sqrt{T_e/m_i}/\Omega_i$, with m_i indicating the ion mass. The system (1)-(3) is characterized by the two parameters β_e and δ. Indicating with m_e the electron mass, these two parameters are defined as $\beta_e = 8\pi n_0 T_e/B_0^2$ and $\delta = \sqrt{m_e/m_i}$. They correspond to the ratio between the equilibrium internal pressure and the magnetic pressure exerted by the guide field, and to the mass ratio, respectively. The symbol $\nabla_\perp^2 = \partial_{xx} + \partial_{yy}$ refers to the Laplacian operator with respect to the coordinates x and y, whereas the bracket $[\,,\,]$ is defined by $[f, g] = \partial_x f \partial_y g - \partial_y f \partial_x g$ for two functions f and g.

The system (1)-(3) is evidently not closed, as long as one does not provide an expression for the parallel heat flux $q_{\parallel_e}$ in terms of lower order moments. For the present analysis, we will consider two possible closures. The first one corresponds to the adiabatic closure

$$q_{\parallel_e} = 0. \tag{5}$$

In this case the heat transport along the magnetic field lines is neglected and the resulting system possesses a Hamiltonian structure [36].

The second closure is given by

$$q_{\parallel_e} = -\frac{2}{\delta}\sqrt{\frac{2}{\pi}}\mathcal{L}t_{\parallel_e}. \tag{6}$$

with $\mathcal{L}$ an operator accounting for the Landau damping. More precisely, we follow the Landau closure previously implemented in Ref. [36] and derived from Refs. [17, 27, 34]. When periodic boundary conditions are imposed along the x and y directions we can indicate with $f(x, y, t) = \sum_{\mathbf{k}=-\infty}^{+\infty} f_{\mathbf{k}}(t) \exp(i(k_x x + k_y y))$ the Fourier series for a generic time-dependent function f satisfying periodic boundary conditions over $\mathcal{D}$. The symbol $\mathbf{k}$ is defined by $\mathbf{k} = (k_x, k_y)$ where $k_x = \pi p/L_x$ and $k_y = \pi m/L_y$ are the wave numbers along the x and y direction, respectively, with $p, m \in \mathbb{Z}$. In the present two-dimensional setting, the action of

the operator $\mathcal{L}$ on a function f is given by $\mathcal{L}f(x,y,t) = \sum_{\mathbf{k}=-\infty}^{+\infty} (\mathcal{L}f)_{\mathbf{k}}(t) \exp(i(k_x x + k_y y))$ where

$$(\mathcal{L}f)_{\mathbf{k}}(t) = -[(\mathbf{k}_0 \cdot \bar{\tau} \cdot \mathbf{k}_0)^{-1/2}][A_{\parallel}, f]_{\mathbf{k}}(t). \tag{7}$$

In Eq. (7), $\bar{\tau} = \langle \mathbf{b} \otimes \mathbf{b} \rangle$ with $\langle\, \rangle$ indicating the spatial average over the domain $\mathcal{D}$ and $\mathbf{b} = \mathbf{B}/|\mathbf{B}|$. We indicate with $\mathbf{k}_0$ the vector $(k_x, k_y, 0)$ and with $[A_{\parallel}, f]_{\mathbf{k}}(t)$ the Fourier coefficient, associated with the wave number $\mathbf{k}$, of the Fourier series of the function $[A_{\parallel}, f](x,y,t)$. The expression (7) descends from the original formulation of the Landau closure of Ref. [33] and applies, as mentioned above, to the case where periodic boundary conditions are imposed along both the x and y directions. In the present analysis, however, periodic boundary conditions will be imposed only along the y direction. Also, the ordering on which the model (1)-(3) is based, admits only quadratic nonlinearities. Therefore, as already applied in Ref. [36], a variant of the expression (7), specified in Sec. III A, will be adopted.

The model (1)-(3) applies to collisionless plasmas with $\beta_e \sim \delta^2 \ll 1$. Ions are assumed to be cold and the characteristic frequency of the phenomena under consideration has to be much smaller than the ion cyclotron frequency Ω_i. For the derivation of the model we refer to Ref. [36], where the model is obtained from the more general gyrofluid model of Ref. [33] by making use of an asymptotic ordering. Eq. (1) can be seen as the evolution equation for the vorticity $\nabla_\perp^2 \varphi$ associated with the $\mathbf{E} \times \mathbf{B}$ velocity $\mathbf{v}_{\mathbf{E}\times\mathbf{B}} = \hat{z} \times \nabla\varphi$. From the quasi-neutrality equation, it follows that for this model the relation $n_e = \nabla_\perp^2 \varphi$ holds [36], with n_e indicating the fluctuations of the electron density with respect to the equilibrium value n_0. Therefore, Eq. (1) can also be seen as a continuity equation for the electron species. Eq. (2) corresponds to the parallel electron momentum equation or, equivalently, to the parallel Ohm's law, where the terms associated with the electron inertia, i.e. those multiplied by the coefficient δ^2, break the frozen-in condition and allow for MR. Finally, Eq. (3) governs the evolution of the parallel electron temperature. Perpendicular electron temperature fluctuations as well a fluctuations of the ion gyrofluid moments are neglected.

III. SIMULATION RESULTS AND ANALYSIS

A. Numerical setup

We solve numerically the system (1)-(3) (adopting the closure (5) or (6)) over the domain $\mathcal{D}$ with $L_x = 46.26$ and $L_y = 12\pi$. The initial condition on the fields φ, $A_\parallel$ and $t_{\parallel_e}$ corresponds to

$$\varphi(x,y,0) = 0, \qquad A_\parallel(x,y,0) = A_{eq}(x) + A_0\left(\frac{x-x_s}{\lambda}\right)\exp(ik_y y) + c.c., \qquad t_{\parallel_e}(x,y,0) = 0. \tag{8}$$

In Eq. (8), $A_{eq}(x) = -A\ln\cosh(x/\lambda) + \alpha x$, where A, $\lambda > 0$ and α are three constant parameters. The function A_{eq} is the equilibrium magnetic flux function, which yields the following asymmetric sheared component of the equilibrium magnetic field:

$$\mathbf{B}_{eq}(x) = \nabla A_{eq}(x) \times \hat{z} = \left(\frac{A}{\lambda}\tanh\left(\frac{x}{\lambda}\right) - \alpha\right)\hat{y}, \tag{9}$$

where $\hat{y}$ is the unit vector along the y direction. The parameter A is the amplitude of the equilibrium magnetic field, while λ and α control its scale of variation and asymmetry, respectively. In the numerical simulations, the mode number m, associated with the wave number k_y of the initial perturbation, has been fixed by the condition $m = 1$. We indicate with $x = x_s$ the position of the resonant surface which, in this 2D setting, is identified by the condition $k_y B_{eq}(x_s) = 0$, i.e. by

$$x_s = \lambda\,\mathrm{arctanh}\left(\frac{\lambda\alpha}{A}\right). \tag{10}$$

In particular, for $\alpha = 0$ one recovers a symmetric equilibrium, with the resonant surface at $x = 0$, equidistant from the boundaries $x = L_x$ and $x = -L_x$. For $\alpha \neq 0$ one obtains an asymmetric equilibrium, in which the equilibrium parallel current density (whose amplitude is given by $j_{eq}(x) = -(d^2A_{eq}/dx^2)(x) = -A/(\lambda^2\cosh^2(x/\lambda))$) does not have an extremum value at the resonant surface. We recall that a 2D problem for fields depending on x, y and t with an asymmetric equilibrium such as that of Eq. (9), can also be mapped to a single-helicity problem with fields depending on x, $y + \alpha z$ and t, where $\alpha = k_z/k_y$, and k_z

indicates the wave number of the perturbation along the z direction [5] . We recall, however, that the three-dimensional (3D) extension of the model (1)-(3) requires $|\alpha| \ll 1$.

In Eq. (8) we also indicated with A_0 a function, peaked around $(x - x_s)/\lambda = 0$, which determines the profile of the amplitude of the perturbation.

At a given time t, the values of the fields correspond to $\varphi(x, y, t) = \tilde{\varphi}(x, y, t)$, $A_\parallel(x, y, t) = A_{eq}(x) + \tilde{A}_\parallel(x, y, t)$ and $t_{\parallel_e}(x, y, t) = \tilde{t}_{\parallel e}(x, y, t)$, where $\tilde{\varphi}$, $\tilde{A}_\parallel$ and $\tilde{t}_{\parallel e}$ indicate the perturbations of the fields, which satisfy the relation $\tilde{\varphi}(x, y, 0) = \tilde{t}_{\parallel e}(x, y, 0) = 0$ and $\tilde{A}_\parallel(x, y, 0) = A_0((x - x_s)/\lambda) \exp(ik_y y) + c.c.$. We impose that such perturbations vanish at $x = -L_x$ and $x = L_x$ and that they are periodic along the y direction.

As anticipated in Sec. II, a variant of the original Landau closure (6), adapted to this model, is used for non-adiabatic simulations. This form respects the requirement on quadratic nonlinearities and permits to apply the operator $\mathcal{L}$ to functions which are periodic only along the y direction. The explicit expression of the operator can be provided in terms of the coefficients of the Fourier series of the function $\mathcal{L}f(x, y, t)$. The expression for the generic Fourier coefficient associated with the wave number k_y is given by

$$(\mathcal{L}f)_{k_y}(x, t) = \\ = \frac{1}{\sqrt{(A^2/\lambda^2 - (A^2/(\lambda L_x)) \tanh(L_x/\lambda) + \alpha^2) k_y^2}} \left((A/\lambda) \tanh(x/\lambda) - \alpha) i k_y\right) f_{k_y}(x, t). \quad (11)$$

The expression (11) is analogous to the one adopted in Ref. [36] and is obtained from the original expression (7) by removing nonlinearities in the perturbations, by adopting the expression (9) for the magnetic equilibrium and by using differential operators in the real space along the x coordinate.

Simulations have been carried out with the numerical code described in Ref. [36]. This code is 3D, explicit in time, assuming a third order Adams-Bashfort scheme, and parallelized along both the periodic directions y and z, while a compact finite difference scheme is implemented on a non-equispaced grid along the magnetic field shear direction [36]. For the purpose of this paper the code has been run in the 2D limit, avoiding dependence on the z-direction, while a resolution of $n_y = 960$ grid points has been adopted along the y-direction.

For the x-direction $n_x = 1200$ grid points have been adopted on the non equispaced grid so as to guarantee a resolution of $dx = 0.02$ around $x = 0$, where the secondary instabilitiy takes place.

B. Secondary instability induced by asymmetry in the adiabatic case

We consider first the model (1)-(3) with the adiabatic closure (5).

We fix the values of the parameters δ and β_e by setting $\delta = 0.1$ and $\beta_e = 0.05$. The values of these two parameters were not changed throughout the whole paper because we focused on the dependence on parameters characterizing the equilibrium magnetic field and, in particular, its asymmetry.

We begin our analysis illustrating the results from a simulation of an asymmetric case with the following parameters: $A = 1$, $\alpha = 1/4$, $\lambda = 3$. In this Subsection, these results will be presented in comparison with a symmetric case possessing the same values of the parameters except for $\alpha = 0$. In Fig. 1 a comparison of the growth of the perturbed magnetic flux at the X-point, $A_{\parallel X}$, in the two cases, is shown, up to the nonlinear stage when the saturation of the magnetic island is reached. Note that the symmetric and asymmetric case differ in the initial x coordinate of the X-points, which are at $x = 0$ and $x = 2.92$ respectively. The simulation times have been rescaled in order to start with the same amplitude. The perturbed magnetic flux $A_{\parallel X}$ provides also a measure of the linear growth rate. We see then that the asymmetry causes a decrease of the growth rate. Incidentally we mention (although we do not show it here) that for the $m = 1$ mode considered here, which is the most unstable one for our equilibrium configuration, we observe in general a decrease of the growth rate as the value of the asymmetry parameter increases. We point out that linearly this is not true for the less unstable modes, as shown in Ref. [6]. In the same plot we show also the drift, present in the asymmetric case, of the X-point location from the initial position at $x = 2.92$ towards $x = 0$.

The drift along the x-direction can be clarified by equating the time evolution, in the

Lagrangian and Eulerian frames of reference, of the generalized magnetic flux function $F = A_\parallel - \frac{2}{\beta_e}\delta^2\nabla_\perp^2 A_\parallel$, evaluated at the magnetic island X-point of coordinates $(x_X(t), y_X(t))$. This yields

$$\frac{dF(x_X(t), y_X(t), t)}{dt} = \frac{\partial F(x, y, t)}{\partial t}|_X + \mathbf{v}_X \cdot \nabla F|_X \tag{12}$$

where the subscript X indicates the value of the field at the istantaneous position of the $X-$ point and $\mathbf{v}_X$ is the drift velocity of the X-point.

At each time, the eq. (2), evaluated at the X-point, reads as

$$\frac{\partial F(x, y, t)}{\partial t}|_X = -[\varphi, F]|_X \tag{13}$$

where $[A_\parallel, \nabla_\perp^2\varphi]|_X = [A_\parallel, t_{\parallel_e}]|_X = 0$ because of the cancellation of the reconnecting component of the magnetic field at the X-point, i.e. $\nabla A_\parallel(x, y, t) \times \hat{z}|_X = 0$. Since the magnetic flux $A_\parallel$ is an even function of y it follows that the first derivative of F along y vanishes at the magnetic field null point. Hence the X-point position varies only with respect to the x-coordinate, and its velocity along the x direction, denoted as v_{Xx}, becomes

$$v_{Xx} = \left(\frac{dF(x_X(t), y_X(t), t)}{dt} + [\varphi, F]|_X\right)\left(\frac{\partial F}{\partial x}|_X\right)^{-1} \tag{14}$$

Note that, in the symmetric case, the denominator $\partial F/\partial x|_X$ in Eq. (14) vanishes, which means that also the numerator must be zero for the relation not to become singular. This condition is fulfilled only for a constant value of the X-point position.

The blue circle in Fig. 1 shows the time evolution of the X-point position according to the theoretical prediction obtained at each time step by the relation $x_X(t + \Delta t) = x_X(t) + v_{Xx}(t)\Delta t$. The agreement with the the curve obtained from the simulation is quite relevant as long as the fields exhibit a rather smooth nonlinear behavior, while the post-processing evaluation of the field gradients (which appear at the denominator of Eq. (14) across the X-line are not reliable any more in the advanced nonlinear phase.

The reader might be surprised by the abrupt jump in the position of the X-point visible at around $t = 330$ in Fig. 1. We claim that this displacement is a consequence of the nonlinear evolution, described later on in this section, in which the turbulence propagating

along the separatrix has reached the X-point.

In Fig. 2 we show a comparison between the contour plots of the vorticity for the asymmetric and symmetric cases at a comparable time in terms of the island width. The current densities, not shown here, have analogous distribution. It is worth mentioning that in the low β_e regime considered here the current density and vorticity layers are coupled together and undergo a similar nonlinear evolution [9, 15]. Contour plots show that, in both cases, vorticity tends to concentrate along the separatrices of the magnetic island, although the asymmetry leads to an island with a D-shaped structure. In the symmetric case the *phase mixing* process of the Lagrangian invariants associated with the infinite families of Casimirs, characterizing the adiabatic and isothermal limits of this model [16], generates laminar vorticity layers also inside the magnetic island, as the nonlinear evolution proceeds. This is no longer true in the asymmetric case, where the layers remain concentrated mainly along the separatrix. Moreover, as the color bar reveals, the asymmetric vorticity layers are more intense. This latter feature can be better appreciated when analyzing the velocity fields shown in Fig. 3. In the top right panel of Fig. 3 the profiles, for the asymmetric case, of the x and y components of the velocity field $\mathbf{v} = \mathbf{v}_{\mathbf{E}\times\mathbf{B}} = \hat{z} \times \nabla\varphi$ are plotted as a function of x at $y = 10$ in comparison with the symmetric case (left top panel). The dashed lines represent the location of the two branches of the separatrix for the chosen y value. We first highlight the difference between the peaks in the v_y profiles. In the symmetric case they are larger and contained within the island, while in the asymmetric case the profile of v_y is more peaked on the lower branch of the separatrix (the one located at a position with x slightly less than $x = 0$), where the thinnest velocity layers appear. Second, focusing on this layer close to $x = 0$, we observe that the v_y profile is steeper in the inner side of the magnetic island with respect to the outer side. The shape of this peak resembles a kind of asymmetric Bickley jet which, according to the shear flow instability theory [4], may be prone to the KH instability. We recall that the Bickley jet, defined as $v_y(x) = 1/\cosh(x)^2$, is the standard shear flow adopted in fluid mechanics for studying the onset of the KH instability. According to the linear theory, in absence of magnetic field this jet is unstable for any wave

vector below a marginal value. However, in the case of a magnetized plasma a stabilizing role can be exerted by a magnetic field parallel to the flow. In this case in fact the plasma motion associated with the instability is counteracted by the tension that is developed by the distortion of magnetic field lines trapped into the plasma. As a consequence for an ideal plasma when the jet is embedded in a sheared magnetic field like $B_y(x) = B_0 \tanh(x)$ the linear growth rate of the KH instability progressively decreases with increasing B_0, up to a critical value, as well as the number of linearly unstable modes, both at small and high k_y. In the nonlinear regime, even for field intensities significantly below the critical threshold derived in the linear limit, the stabilizing effect is dramatic.

In the bottom panel of Fig. 3 the profiles of the x and y components of the magnetic field are also plotted. We observe that, as expected, the B_x component is almost negligible inside the magnetic island in both the symmetric and asymmetric case. On the contrary the absolute value of the B_y component has a different behavior. In the symmetric case it has comparable values on the two sides of the lower branch of the separatrix, while in the asymmetric case it shows a steep gradient through the lower branch itself dropping to almost a constant value inside the island. This balance between the velocity and magnetic fields justifies the onset of the KH instability [4], that we observe later on in the nonlinear evolution, on the side of the layer facing the inner part of the magnetic island where the stabilizing effect of B_y is weaker.

The development of the KH instability is illustrated by three snapshots taken at subsequent times in Fig. 4 and by the movie provided in the supplemental material. From the dynamical point of view the velocity layers can be seen as counter streaming plasma jets starting from the X-point and propagating at the beginning towards $y = 0$, where they collide forming vortices. Subsequently, jets propagate backward towards the X-point undergoing KH instability, which increases the amplitude of the vortices. When the first vortex has reached the X-point we observe an acceleration of the process of vortex formation and propagation. Moreover the vortices start propagating also on the other branch of the separatrix, where they are stretched by the more intense magnetic field. The current density layers, not shown

here, exhibit a similar behavior.

This indicates a crucial difference with respect to the symmetric case. We point out that the values of the parameters correspond to a regime where $\rho_s/d_e = \sqrt{\beta_e/(2\delta^2)} \approx 1.6$. According to previous analyses [9–11, 14] in such regime with $\rho_s \geq d_e$, even though the current density and vorticity fields exhibit small scale structures, in the symmetric case their behavior remains laminar, as in Fig. 2(a), throughout the whole nonlinear evolution and no secondary instabilities develop. Also, we remark that here we are adopting an adiabatic closure, unlike Refs. [9–11, 14], where an isothermal closure was assumed for the electron fluid. When the same initial conditions, as is the case here, are considered for $\nabla_\perp^2\varphi$ and $t_{\parallel_e}$, the solution $t_{\parallel_e} = 2\nabla_\perp^2\varphi$ can be taken for the system (1)-(3) with $q_{\parallel_e} = 0$. Replacing this solution in the last term of Eq. (2) casts the system in the form

$$\frac{\partial \nabla_\perp^2 \varphi}{\partial t} + [\varphi, \nabla_\perp^2 \varphi] - \frac{2}{\beta_e}[A_\parallel, \nabla_\perp^2 A_\parallel] = 0, \tag{15}$$

$$\frac{\partial}{\partial t}\left(A_\parallel - \frac{2}{\beta_e}\delta^2 \nabla_\perp^2 A_\parallel\right) + [\varphi, A_\parallel - \frac{2}{\beta_e}\delta^2 \nabla_\perp^2 A_\parallel] + 3[A_\parallel, \nabla_\perp^2 \varphi] = 0. \tag{16}$$

This form differs from that of the isothermal system (which descends from replacing Eq. (3) with $t_{\parallel_e} = 0$) by the factor 3 that multiplies the last term on the left-hand side of Eq. (16). This term is denoted as the electron compressibility term and is the one responsible for suppressing the secondary instability in the cases studied in Refs. [9–11, 14]. With the adiabatic assumption, the relative strength of this term is thus even greater than in the isothermal case. In spite of this, the asymmetry appears to be able to overcome the damping effect associated with this term.

We remark that a secondary KH instability was indeed observed also in the symmetric case but in a different regime of the physical parameters, more precisely in the cold electron limit, where $\rho_s/d_e << 1$. In the latter case, however, the head of the colliding jets have a typical symmetric (mushroom) shape (see for instance Ref. [9]). These jets collide at the O-point and then propagate along a direction perpendicular to the initial one. This behavior is inhibited in the asymmetric configuration, where only one side of the jets exhibits vortex formation and cannot propagate outward the separatrix, but is forced to move along the

separatrix itself.

In Fig. 7 a snapshot of the advanced nonlinear phase shows that the turbulent behavior spreads out of the magnetic island when the deformation of the magnetic island separatrix at the O-point latitude is faster than the dynamics of the vorticity layers, which temporarily remain outside the island before being reabsorbed at later times. This vortices motion through the magnetic island separatrix opens a new transport scenario as suggested also in Refs. [18, 19, 30].

In Ref. [19] the electron KH instability was the mechanism allowing for the transport of particles, while in Refs. [18, 30] the authors suggested that the transport of particles from the solar wind across the magnetopause into the magnetosphere is favoured by the turbulence generated by the lower hybrid drift instability driven by the steep density gradients at the magnetopause. We recall that in the cold ion limit adopted here the electron density coincides with the vorticity [36], which also exhibits steep gradients, associated with the above described velocity profiles that generate the KH instability leading to turbulence in our model. We also note that previous 2D simulations described in the literature report a very weak turbulence [18, 30] around the separatrix. Here we have shown that also in 2D configurations a significant level of turbulence may arise in the presence of a strongly asymmetric configuration.

C. Role of the location of the rational surface

We stress that the secondary KH instability previously observed in the asymmetric case is purely due to the geometry of the equilibrium magnetic field, α being the only parameter that has been changed between the two cases presented so far. Nonetheless we observed that, in general, a finite value of α is a necessary but not sufficient condition to trigger this instability. Indeed we performed different simulations keeping the same values of $\delta = 0.1$ and $\beta_e = 0.05$, but varying α, λ and the equilibrium magnetic field amplitude A. The results are summarized in Table I and discussed hereafter. By keeping $A = 1, \lambda = 3$ but

with $\alpha = 1/8$, i.e. by decreasing the value of the asymmetry parameter α with respect to the previously investigated asymmetric case, no instability has been found. This shows that, as above anticipated, a finite value of α is not sufficient to trigger the instability. Assuming $A = 1.35$, but keeping $\alpha = 1/4$ and $\lambda = 3$ we do not find any instability either, which indicates that the amplitude of the equilibrium magnetic field can suppress the instability. A simulation with $A = 1$, $\lambda = 3$ and $\alpha = 6/25$ shows the occurrence of the KH instability, confirming the crucial role of the α parameter. The simulations with $A = 0.67$, $\lambda = 2$, $\alpha = 1/4$, and $A = 0.33$, $\lambda = 1$, $\alpha = 1/4$ lead again to the occurrence of the KH instability. We note that all the parameters α, A and λ contribute to the definition of the location of the resonant surface given in Eq. (10). However, the data in the fourth column of Table I show that the value of the distance of the rational surface from the location of the current density peak alone is not sufficient to determine whether the instability takes place or not. Indeed, the last case in the table exhibits the KH instability but is characterized by a value $x_s = 0.97$, smaller than the values of x_s of the second and third cases, which did not lead to a KH instability. It emerges that, among the seven cases discussed here, only those that have a value of x_s/λ sufficiently large, exhibit the turbulent behavior induced by the instability, while the other cases persist in a laminar behavior throughout all the advanced nonlinear phase. To understand the physical reason of the observed difference, it is interesting to compare the profiles of the y-component of the velocity field shown in Fig. 5 for different values of the resonant surface of the corresponding equilibrium. In particular, we selected one stable case and two cases leading to instability. The profiles have been normalized to their maximum value and have been shifted along the x axis in such a way that their maxima are located at the same value of the x coordinate. We note that, as the resonant surface goes further away from $x = 0$, the width of the peak narrows and the gradient on the right side becomes steeper. In particular, this makes the part of the layer inside the magnetic island more prone to the KH instability as the value of x_s/λ exceeds a certain threshold, in agreement with the subsequent development of the instability shown by the simulations.

α	λ	A	x_s	x_s/λ	KH inst.
0	3	1	0	0	No
$\frac{1}{8}$	3	1	1.18	0.39	No
$\frac{1}{4}$	3	1.35	1.88	0.63	No
$\frac{6}{25}$	3	1	2.72	0.91	Yes
$\frac{1}{4}$	2	0.67	1.95	0.97	Yes
$\frac{1}{4}$	3	1	2.92	0.97	Yes
$\frac{1}{4}$	1	0.33	0.97	0.97	Yes

TABLE I: Table summarizing whether the secondary KH instability occurs or not, depending on the values of the equilibrium parameters α, λ and A, on the location of the resonant surface x_s and on the ratio x_s/λ. One observes that the instability takes place if x_s/λ is sufficiently large.

All these considerations permit to formulate a further condition that must be satisfied for an asymmetric case to develop the KH instability. The resonant surface must be located far enough from the $x = 0$ surface. How to define what is "enough" is a subtle question, which requires a more detailed parametric analysis, which is beyond the scope of this paper. However we note that, for the simulation campaign carried out here, the x_s threshold value is of the order of the equilibrium scale length, i.e. $x_s/\lambda \sim 1$ appears to be an estimate for the instability threshold in the adiabatic case. Although the results reported here have been obtained keeping constant the box length $2L_y = 24\pi$, other simulations carried out with $2L_y = 12\pi$ have shown an analogous behavior.

D. Effect of Landau dissipation on the secondary instabilities

In this Subsection we analyze the effect of the dissipation by switching on the Landau damping term in a simulation with the same parameters of the case with $\alpha = 1/4$ reported in Subsection III B. We recall that $\alpha = 1/4$ corresponds to $k_z = 1/48 \approx 0.021$, according to the mapping with the single helicity problem mentioned in Sec. III A. We confirm that for

such a small value of k_z the effect on the linear growth rate is almost negligible, as already shown in Ref. [36].

The major effects of the Landau damping term can be appreciated when looking into the nonlinear phase of the reconnection process, where the presence of dissipation inhibits the secondary instabilities observed in the adiabatic case. Indeed the evolution of the vorticity field remains laminar until the end of the simulation. In Fig. 6 a comparison of the y component of the velocity profiles is shown for the two cases under consideration, at a time just before the onset of the KH instability occurring in the adiabatic case. The profiles have been normalized to their maximum. It is clear that the Landau effect prevents the velocity peaks from narrowing and smooths their gradients across the separatrix (dashed line), thus eliminating the conditions that make the colliding jet unstable to the KH instability.

We find it appropriate also to comment our results with respect to the role played by the invariants that the model possesses in the adiabatic limit and whose conservation is violated by the presence of the Landau term. Indeed, the model (1)-(3), in the adiabatic limit $q_{\parallel_e} = 0$ can be cast in the form [36]

$$\frac{\partial \nu_+}{\partial t} + [\varphi_+, \nu_+] = 0, \tag{17}$$

$$\frac{\partial \nu_-}{\partial t} + [\varphi_-, \nu_-] = 0, \tag{18}$$

$$\frac{\partial s}{\partial t} + [\varphi, s] = 0, \tag{19}$$

where

$$\nu_\pm = A_\parallel - \frac{2}{\beta_e}\delta^2 \nabla_\perp^2 A_\parallel \pm \frac{\delta}{\sqrt{3}}(\nabla_\perp^2 \varphi + t_{\parallel_e}), \qquad s = \nabla_\perp^2 \varphi - \frac{t_{\parallel_e}}{2}, \tag{20}$$

$$\varphi_\pm = \varphi \pm \frac{\sqrt{3}}{\delta} A_\parallel. \tag{21}$$

The fields $\nu_\pm$ and s correspond to Lagrangian invariants advected by generalized incompressible velocity fields. The presence of such Lagrangian invariants is associated with the existence of infinite families of Casimir invariants given by

$$\mathcal{C}_\pm = \int d^2x \, f_\pm(\nu_\pm), \qquad \mathcal{C} = \int d^2x \, f(s), \tag{22}$$

where $f_\pm$ and f are arbitrary functions. In particular, for the initial conditions considered in the present analysis, as already mentioned, the relation $t_{\parallel_e} = 2\nabla_\perp^2\varphi$ holds. In this case one has

$$\nu_\pm = A_\parallel - \frac{2}{\beta_e}\delta^2\nabla_\perp^2 A_\parallel \pm \sqrt{3}\delta\nabla_\perp^2\varphi, \qquad s = 0, \tag{23}$$

$$\varphi_\pm = \varphi \pm \frac{\sqrt{3}}{\delta}A_\parallel. \tag{24}$$

Thus, only the two Lagrangian invariants $\nu_\pm$ lead to a non trivial dynamics. In previous works, such as those of Refs. [11, 16], the isothermal two-field model reduction of our three-field model was used. Such two-field model also admits a reformulation in terms of two Lagrangian invariants analogous to $\nu_\pm$. In these References it was shown that the system tends to form small scale structures concentrated in particular along the separatrices of the magnetic island, caused by the phase mixing process of these invariants. This prevents the formation of strong gradients representing the necessary condition for a secondary KH-like instability. However, when the system cannot be completely reformulated in terms of advection equations for Lagrangian invariants, for instance due to the assumption of cold electrons [9] or of higher β_e [15, 37], the secondary instability can take place. Our conclusion in Sec. III B can then be re-expressed in this context, stating that a secondary KH-like instability can take place even if the system can be recast in the form of advection equations for Lagrangian invariants. This can happen if a sufficiently asymmetric equilibrium (in the sense described in Sec. III B) is adopted.

On the other hand, in the presence of the Landau damping term, a reformulation of the model in the form (17)-(19) is no longer possible. For instance, one can easily see that the Landau term tends to damp temperature fluctuations, without affecting in the same manner the vorticity [36]. As a consequence, the difference between $t_{\parallel_e}$ and $\nabla_\perp^2\varphi$ is no longer constant along the flow, which expresses the fact that s is no longer a Lagrangian invariant. As mentioned above, the Landau damping term appears to inhibit the KH instability. Clearly, this inhibition is of different nature with respect to that due to the phase mixing of the Lagrangian invariants observed in the symmetric case as it is due to the smoothing of

the velocity gradients that form in the asymmetric adiabatic case.

In order to have an estimate of the impact of Landau damping on the non-conservation of Casimir invariants, we considered the temporal evolution of the quantities $\int d^2x\,\nu+$ and $\int d^2x\,\nu_+^2$ both in the adiabatic and Landau case. Because these two integral quantities are of the form $\mathcal{C}_+$ indicated in Eq. (22), they are Casimir invariants in the adiabatic limit. It turns out that, for our choice of the equilibrium parameters, the conservation of the quantities $\int d^2x\,\nu_+$ and $\int d^2x\,\nu_+^2$ does not differ significantly between the adiabatic and the Landau cases. As shown in Fig. 8, the curves are almost coincident. This behavior reflects also in the feeble differences between the energy distributions (not shown here) and mainly depends on the strength of the sheared equilibrium magnetic field (for a higher equilibrium magnetic field strength the Landau damping effect on the energy is more evident, see [36]). However, while the Landau damping seems not to play a significant role in the conservation of integral quantities, it significantly affects the plasma behavior locally by preventing the Kelvin-Helmoltz instability onset.

Finally, we would like to point out that the linearized Landau-fluid model exhibits a very good agreement, in terms of the estimation of the linear growth rates for reconnecting modes, with the analytical theory based on a hybrid fluid-kinetic model [36]. This could justify the choice of the Landau-fluid closure as an effort in the direction of providing fluid models retaining features of the kinetic theory. On the other hand, the quality of the agreement between the Landau-fluid and the kinetic dynamics in the nonlinear phase is a more delicate issue. Also, when considering the present Landau-fluid model as a step toward kinetic models, it should be pointed out that, as mentioned above, the Landau damping term in the fluid model breaks the Hamiltonian structure, which, on the other hand, is present in the drift-kinetic model from which the Landau-fluid model can be derived. In particular, as shown in Ref. [21], according to a Hamiltonian drift-kinetic model, the phase space of gyrocenters can be foliated into leaves, each hosting a dynamics analogous to that of the Lagrangian invariants of the fluid model takes place. Thus, although the Landau-fluid closure provides in general a better matching with the linear kinetic theory with respect to the

adiabatic closure, one has to be aware of possible discrepancies emerging in the advanced nonlinear phase.

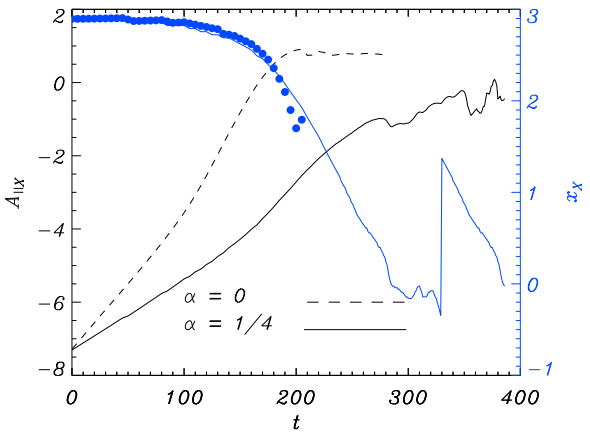

FIG. 1: Time evolution of the perturbed magnetic flux at the X-point for the symmetric (dashed line) and the asymmetric case (solid line). The presence of asymmetry decreases the linear growth rate. The drift along the x coordinate (represented on the right axis) of the X-point location is plotted in blue. This drift, typical of the asymmetric case, shows how the X-point tends to migrate toward the $x = 0$ line. The blue circles represent the approximation of the X-point displacement according to the velocity field in Eq. (14). The fit between the curves is restricted to a limited section of the total simulated time, because the post-processing treatement of the data does not allow a reliable evaluation of the F field gradient across the X-line (which appear at the denominator of the Eq. (14)) in the advanced nonlinear phase.

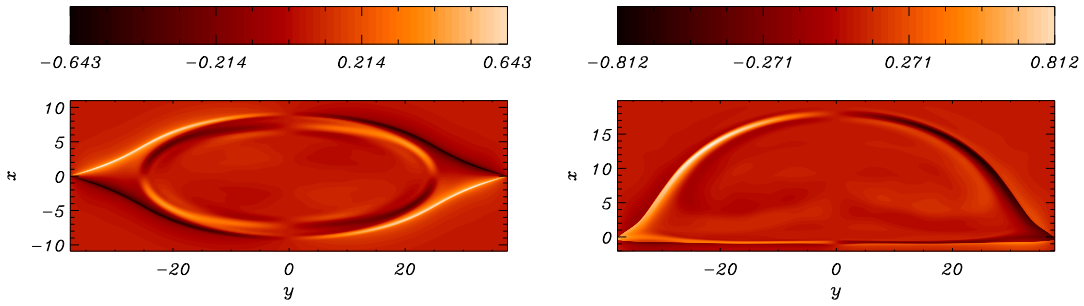

(a) (b)

FIG. 2: Contour plots of the vorticity $\nabla^2_\perp \varphi$, at comparable times in terms of the island width, for different values of the asymmetry parameters. The left panel corresponds to a symmetric case, $\alpha = 0$, while the right panel corresponds to an asymmetric case with $\alpha = 1/4$. In both cases vorticity concentrates along the separatrices but in the symmetric case an elliptic structure is visible also inside the island. Note that the asymmetric layers are more intense.

IV. CONCLUSIONS

In this paper we analyzed how the intense vorticity layers, that form when a MR event takes place, evolve in an asymmetric low β_e 2D configuration. In the finite electron temperature regime with $\rho_s/d_e > 1$ that we considered here, these layers are aligned along the separatrices of the magnetic island and have a laminar behavior in the symmetric configuration [11]. We have shown that this paradigm breaks down when an asymmetric equilibrium

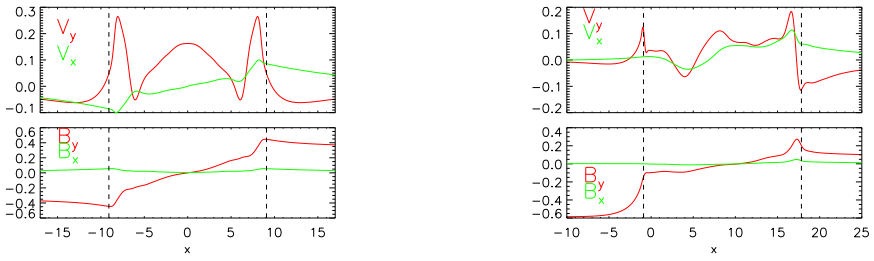

(a) (b)

FIG. 3: Profiles of v_x, v_y (top panels), B_x and B_y (bottom panels) plotted as a function of x at $y = 10$. The symmetric case, $\alpha = 0$, is on the left and the asymmetric case, $\alpha = 1/4$, is on the right. The dashed lines represent the location of the two branches of the separatrix for the chosen y value.

magnetic field is taken into account. In the asymmetric configuration the vorticity may undergo a secondary instability of the KH type, which drives a turbulent plasma behavior around the magnetic island. In this case the velocity gradients, which develop firstly along the branch of the separatrix close to the $x = 0$ axis, tend to peak like an asymmetric Bickley jet that is well known to be prone to secondary instabilities. However, the presence of an asymmetry in the equilibrium configuration turns out to be a necessary but not sufficient condition for the occurrence of secondary instabilities. We have shown that the actual driving parameter for the onset of such an instability depends on the radial position of the resonant surface in the linear phase, *i.e.* in our 2D setting, where the sheared component of the equilibrium magnetic field goes to zero. In particular, for the instability to take place, the value of the rational surface, x_s, must be of the order of the equilibrium scale length.

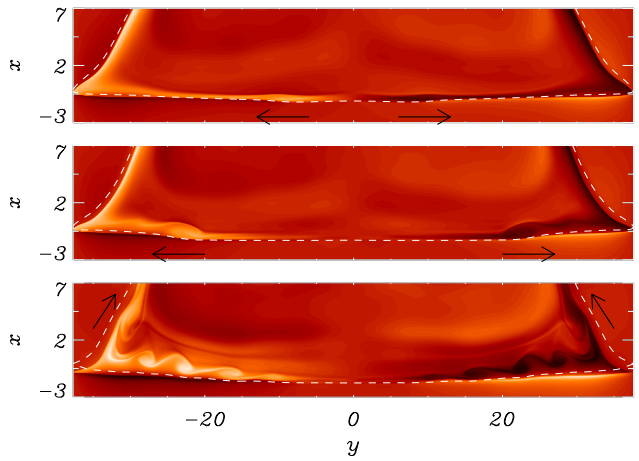

FIG. 4: Contour plots of the vorticity at three subsequent times: $t = 300$ (top frame), $t = 306$ (middle frame), $t = 318$ (bottom frame). The arrows indicate the direction of propagation of the instability front. The dashed line in each figure shows the magnetic island separatrix at the corresponding time.

Moreover in the asymmetric configuration the turbulence is not confined into the magnetic island but is allowed to spread out of the separatrix, opening transport channels otherwise closed. Our results highlight that a fully developed turbulent behavior can be achieved in 2D asymmetric configurations, differently from previous results mainly obtained with PIC simulations, where a strong turbulent behavior was observed only in 3D settings [18, 30]. We also analyzed the stabilizing effect of a non-adiabatic closure on these secondary insta-

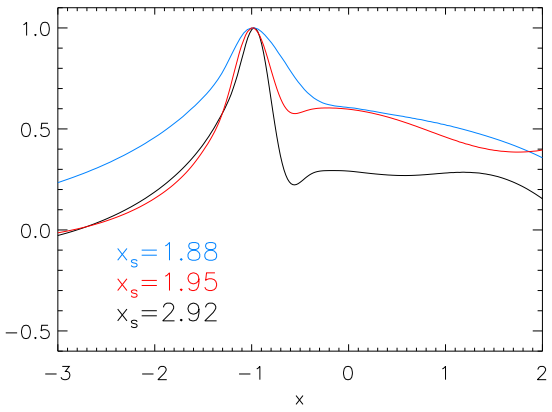

FIG. 5: Profiles of v_y for different values of the resonant surface of the equilibrium magnetic field. The profiles have been normalized to their maximum value and have been shifted along the x axis so that the location of their maxima coincides at the same x coordinate. Note the narrowing of the peak as the value of x_s increases. The cases with $x_s = 1.95$ and $x_s = 2.92$ correspond to values of x_s/λ sufficiently large to yield the KH instability.

bilities, by including a Landau damping term in our model. This term prevents the velocity peaks from narrowing, so inhibiting their destabilization.

In the future we intend to address this problem in a full 3D setting, where several modes can be nonlinearly excited driving a secondary instability on their own. Moreover, the presence of several modes may influence this scenario because of the magnetic chaos that can be

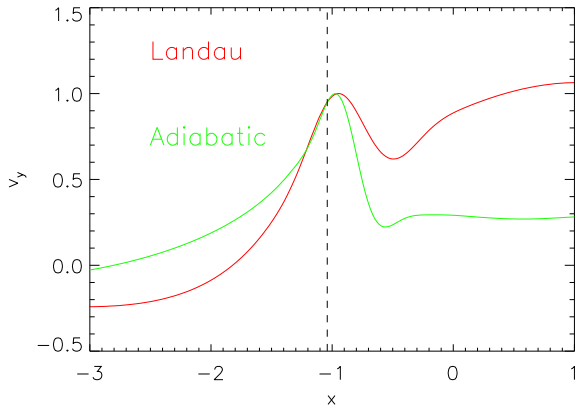

FIG. 6: Profiles of v_y, normalized to their maximum, comparing the effect of the Landau damping term with the adiabatic case. The values of the parameters are $\alpha = 1/4, \lambda = 3, A = 1$ for both cases. The presence of the Landau damping leads to weaker velocity gradients.

generated by their interaction.

Another interesting aspect worth of a deeper attention concerns the particle density, which, in our model, is proportional to the vorticity. In the minimal asymmetric framework where we have described the onset and the behavior of the KH instability, the equilibrium density is uniform and, considering the magnetospheric context, the equilibrium magnetic asymmetry depends only on the direction of the solar wind. In other works with a different equilibrium configuration, equilibrium density gradients are assumed and secondary Rayleigh-Taylor

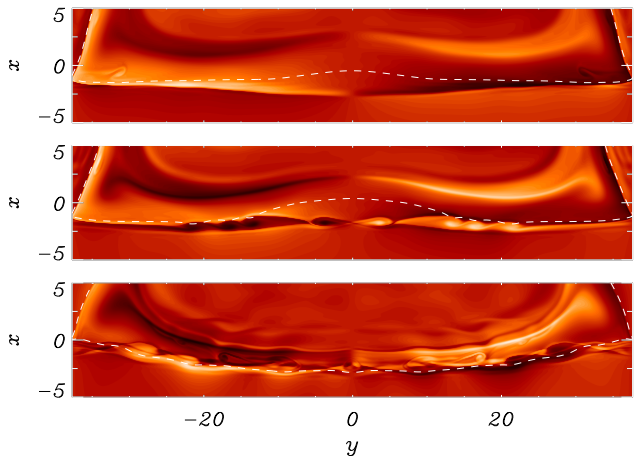

FIG. 7: Contour plots of the vorticity at three subsequent times: $t = 354$ (top frame), $t = 360$ (middle frame), $t = 375$ (bottom frame). The white dashed lines identify the corresponding magnetic island separatrices.

modes associated with the density inhomogeneities are induced by the KH instability in the nonlinear phase ([12, 22] and references therein). In Ref. [12], the role of the small-scale KH structures in the mass transfer between the solar wind and the magnetosphere is also discussed. In this perspective, a further development of our investigation is represented by the particle transport in the turbulent region produced by the KH instability and, in particular, across the island's boundaries, which could be carried out through a test particle approach ([28] and references therein).

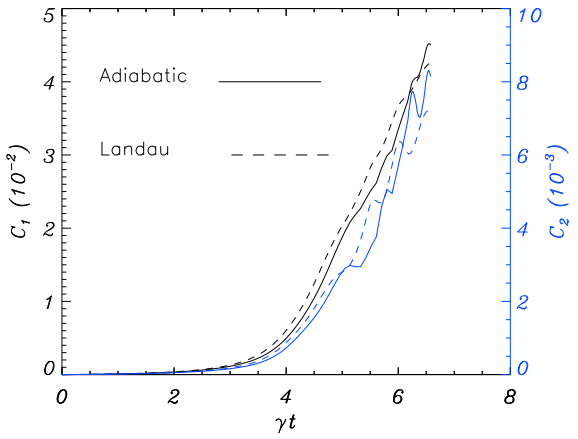

FIG. 8: Time evolution of the quantities $C_1 = \int d^2x\, \nu_+$ (black lines) and $C_2 = \int d^2x\, \nu_+^2$ (blue lines) for the adiabatic (solid lines) and the Landau (dashed lines) cases. The times are normalized with respect to the linear growth rate of the reconnection process. The values of the parameters are $\alpha = 1/4, \lambda = 3, A = 1$ for both cases.

In conclusion, the use of the presently adopted reduced fluid model implies evident limitations, in terms of the range of applicability, when compared to kinetic models. In order to reduce the gap with kinetic descriptions and in view of possible applications to asymmetric reconnection events in the magnetosphere, we also intend to adopt more refined fluid models valid for larger β_e values and including finite ion Larmor radius effects as well as equilibrium temperature anisotropies.

Supplementary material

See the movie in the supplementary material for a complete description of the evolution of the KH instability. The movie shows the time evolution of the vorticity spatial distribution $U(x, y, t) = \nabla^2_\perp \varphi(x, y, t)$ for the case $\alpha = 1/4, A = 1$ and $\lambda = 3$ in the left frame. The superposed dashed lines correspond to the magnetic island separatrices. The time evolution of $A_{\parallel_X}$ is plotted on the right frame, in order to highlight the link between KH and MR instability.

Acknowledgments

Computations have been performed on the Mesocentre SIGAMM machine, hosted by Observatoire de la Côte d'Azur. The authors thank P.L. Sulem and T. Passot for providing useful hints and for discussing the results. DG and DB thank prof. B. Coppi and the Ignitor theory group at CNR for stimulating discussions.

---

[1] Bertin, G. 1982 Effect of local current gradients on magnetic reconnection. *Phys. Rev. A* **25**, 1786.

[2] Birn, J., Drake, J., Shay, M., Rogers, B., Denton, R., Hesse, M., Kuznetsova, M., Ma, Z., Bhattacharjee, A., Otto, A. & Pritchett, P. 2001 Geospace environmental modeling (gem) magnetic reconnection challenge. *J. Geophys. Res.* **106**, 3715.

[3] Biskamp, D. 1997 Collisional and collisionless magnetic reconnection. *Phys. Plasmas* **4**, 1964–1968.

[4] Biskamp, D. 2000 *Magnetic Reconnection in Plasmas*. Cambridge University Press, Cambridge.

[5] Borgogno, D., Grasso, D., Porcelli, F., Califano, F., Pegoraro, F. & Farina, D. 2005 Aspects of three-dimensional magnetic reconnection. *Phys. Plasmas* **12**, 032309.

[6] Borgogno, D., Perona, A. & Grasso, D. 2017 Test-electron analysis of the magnetic reconnection topology. *Phys. Plasmas* **24**, 122303.

[7] Burch, J. L., Torbert, R. B., Phan, T. D., Chen, L.-J., Moore, T. E., Ergun, R. E., Eastwood, J. P., Gershman, D. J., Cassak, P. A., Argall, M. R., Wang, S., Hesse, M., Pollock, C. J., Giles, B. L., Nakamura, R., Mauk, B. H., Fuselier, S. A., Russell, C. T., Strangeway, R. J., Drake, J. F., Shay, M. A., Khotyaintsev, Y. V., Lindqvist, P.-A., Marklund, G., Wilder, F. D., Young, D. T., Torkar, K., Goldstein, J., Dorelli, J. C., Avanov, L. A., Oka, M., Baker, D. N., Jaynes, A. N., Goodrich, K. A., Cohen, I. J., Turner, D. L., Fennell, J. F., Blake, J. B., Clemmons, J., Goldman, M., Newman, D., Petrinec, S. M., Trattner, K. J., Lavraud, B., Reiff, P. H., Baumjohann, W., Magnes, W., Steller, M., Lewis, W., Saito, Y., Coffey, V. & Chandler, M. 2016 Electron-scale measurements of magnetic reconnection in space. *Science* .

[8] Coppi, B., Basu, B., Buratti, P., Cardinali, A. & Gatto, R. 2019 Endogenous and asymmetric magnetic reconnection with assoicated processes of relevance to fusion burning plasmas. *Plasma Phys. and Control. Fusion* p. submitted.

[9] Del Sarto, D., Califano, F. & Pegoraro, F. 2003 Secondary instabilities and vortex formation in collisionless-fluid magnetic reconnection. *Phys. Rev. Lett.* **91**, 235001.

[10] Del Sarto, D., Califano, F. & Pegoraro, F. 2005 . *Phys. Plasmas* **12**, 012317.

[11] Del Sarto, D., Califano, F. & Pegoraro, F. 2006 Electron parallel compressibility in the nonlinear development of two-dimensional collisionless magnetohydrodynamic reconnection. *Mod. Phys. Lett. B* **20**, 931.

[12] Faganello, M. & Califano, F. 2017 Magnetized KelvinHelmholtz instability: theory and simulations in the Earths magnetosphere context. *J. Plasmas Phys.* **83** (6), 535830601.

[13] Furth, H., Killeen, J. & Rosenbluth, M. 1963 Finite resistivity instabilities of a sheet pinch. *Phys. Fluids* **6**, 459.

[14] Grasso, D., Borgogno, D. & Pegoraro, F. 2007 Secondary instabilities in two- and three-dimensional magnetic reconnection in fusion relevant plasmas. *Phys. Plasmas* **14**, 055703.

[15] Grasso, D., Borgogno, D., Pegoraro, F. & Tassi, E. 2009 Coupling between reconnection and Kelvin-Helmholtz instabilities in collisionless plasmas. *Nonlin. Processes Geophys.* **16**, 241.

[16] Grasso, D., Califano, F., Pegoraro, F. & Porcelli, F. 2001 Phase mixing and satu-

ration in Hamiltonian reconnection. *Phys. Rev. Lett.* **86**, 5051–5054.

[17] Kobayashi, S., F., S., Passot, T., Laveder, D., Sulem, P., Huang, S. Y., Henri, P. & Smets, R. 2017 Three-dimensional simulations and spacecraft observations of sub-ion scale turbulence in the solar wind: influence of Landau damping. *Astrophys. J.* **839**, 122.

[18] Le, A., Daughton, W., Chen, L. & Egedal, J. 2017 Enhanced electron mixing and heating in 3d asymmetric reconnection at the earths magnetopause. *Geophys. Res. Lett.* **44**, 2096.

[19] Lee, S.-Y., Lee, E., Kim, K.-H., Lee, D.-H., Seon, J. & Jin, H. 2015 Electron debye scale kelvin-helmholtz instability: Electrostatic particle-in-cell simulations. *Phys. Plasmas* **22**, 122113.

[20] Li, X., Zhang, J., Yang, S., Hou, Y. & Erdly, R. 2018 Observing Kelvin-Helmholtz instability in solar blowout jet. *Scientific Reports* **8** (8136).

[21] Liseikina, T., Pegoraro, F. & Echkina, E. Y. 2004 Foliation and mixing of the electron drift-kinetic distribution function in nonlinear two-dimensional magnetic reconnection. *Phys. Plasmas* **11**, 3535.

[22] Matsumoto, Y. & Hoshino, M. 2004 Onset of turbulence induced by a KelvinHelmholtz vortex. *Geophys. Res. Lett.* **31**, L02807.

[23] Militello, F., Borgogno, D., Grasso, D., Marchetto, C. & Ottaviani, M. 2011 Asymmetric tearing mode in the presence of viscosity. *Phys. Plasmas* **25**, 1786.

[24] Militello, F., Huysmans, G., Ottaviani, M. & Porcelli, F. 2004 Effects of local features of the equilibrium current density profile on linear tearing modes. *Phys. Plasmas* **11**, 125.

[25] Ottaviani, M. & Porcelli, F. 1993 Nonlinera collisionless magnetic reconnection. *Phys. Rev. Lett.* **71**, 3802–3805.

[26] Parker, E. 1957 Sweet's mechanism for merging magnetic fields in conducting fluids. *J. Geophys. Res.* **509–520**, 1964–1968.

[27] Passot, T., Henri, P., Laveder, D. & Sulem, P. L. 2014 A fluid approach for ion scale plasmas with weakly distorted magnetic fields. *Euro. Phys. J. D.* **68**, 207.

[28] Perona, A., Borgogno, D. & Eriksson, L.-G. 2014 A test electron model for the study of three dimensional magnetic reconnection effects. *Comput. Phys. Commun.* **185**, 86.

[29] Phan, T. D., Eastwood, J. P., Shay, M. A., Drake, J. F., Sonnerup, B. U. Ö.,

Fujimoto, M., Cassak, P. A., Øieroset, M., Burch, J. L., Torbert, R. B., Rager, A. C., Dorelli, J. C., Gershman, D. J., Pollock, C., Pyakurel, P. S., Haggerty, C. C., Khotyaintsev, Y., Lavraud, B., Saito, Y., Oka, M., Ergun, R. E., Retino, A., Le Contel, O., Argall, M. R., Giles, B. L., Moore, T. E., Wilder, F. D., Strangeway, R. J., Russell, C. T., Lindqvist, P. A. & Magnes, W. 2018 Electron magnetic reconnection without ion coupling in Earths turbulent magnetosheath. *Nature* (557), 202.

[30] Price, L., Swisdak, M., Drake, J., Cassak, P., Dahlin, J. & Ergun, R. 2016 The effects of turbulence on threedimensional magnetic reconnection at the magnetopause. *Geophys. Res. Lett.* **43**, 6020.

[31] Priest, E. R. & Forbes, T. G. 2000 *Magnetic Reconnection*. Cambridge, Cambridge University Press.

[32] Rosenberg, M., Li, C., Fox, W., Igumenshchev, I., Sguin, F. H., Town, R., Frenje, J. A., Stoeckl, C., Glebov, V. & Petrasso, R. D. 2015 A laboratory study of asymmetric magnetic reconnection in strongly driven plasmas. *Nature Commun.* **6** (6190).

[33] Scott, B. 2010 Derivation via free energy conservation constraints of gyrofluid equations with finite-gyroradius electromagnetic nonlinearities. *Phys. Plasmas* **17**, 102306.

[34] Sulem, P., Passot, T., Laveder, D. & Borgogno, D. 2016 Influence of the Nonlinearity Parameter on the Solar Wind Sub-ion Magnetic Energy Spectrum: FLR-Landau Fluid Simulations. *Astrophys. J.* **818**, 66.

[35] Sweet, P. 1957 The production of high-energy particles in solar flares. *Nuovo Cimento Suppl.* **8, Ser.X**, 188–196.

[36] Tassi, E., Grasso, D., Borgogno, D., Passot, T. & Sulem, P. 2018 A reduced Landau-gyrofluid model for magnetic reconnection driven by electron inertia. *J. Plasma Phys.* **84**, 725840401.

[37] Tassi, E., Morrison, P. J., Grasso, D. & Pegoraro, F. 2010 Hamiltonian four-field model for magnetic reconnection: nonlinear dynamics and extension to three dimensions with externally applied fields. *Nucl. Fusion* **50**, 034007.

[38] Zakharov, L. & Rogers, B. 1992 Twofluid magnetohydrodynamic description of the internal kink mode in tokamaks. *Phys. Fluids B: Phys. Plasmas* **4**, 3285–3301.